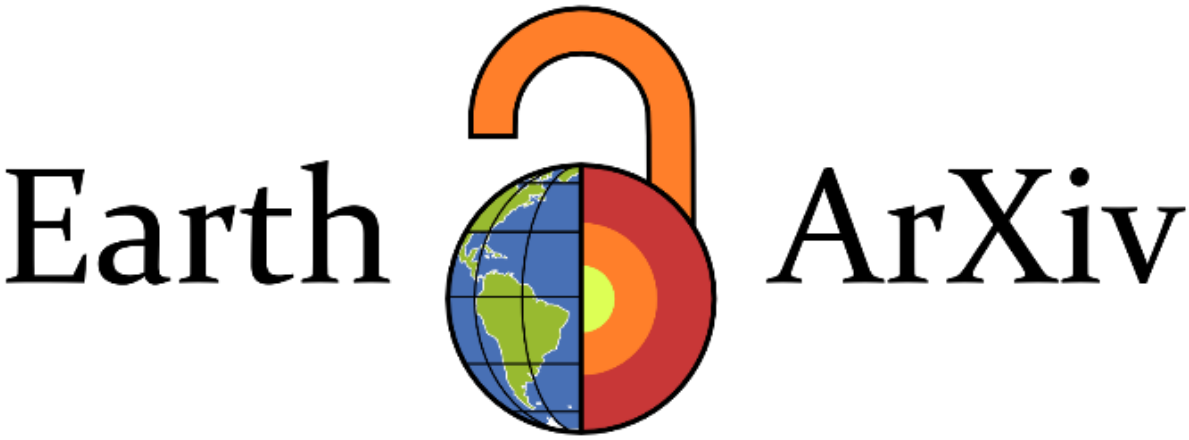

Effects of cementation on the cyclic resistance of granular soils with presence of initial static shear stress

Aoxi Zhang[1*], Chaofa Zhao[2], Hadrien Rattez[3], Frédéric Collin[1]

[1*]Department ArGEnCo - Geotechnique, University of Liège, Liège, 4000,Belgium.
[2]Department of Civil Engineering, Computing Center for Geotechnical Engineering, Zhejiang University, Hangzhou, 310012,China.
[3]Institute of Mechanics, Materials and Civil Engineering, UCLouvain, Louvain-la-Neuve, 1348,Belgium.

*Corresponding author(s). E-mail(s): aoxi.zhang@zju.edu.cn;
Contributing authors: chaofa.zhao@zju.edu.cn; hadrien.rattez@uclouvain.be; f.collin@uliege.be;

Abstract

In engineering applications such as non-invasive cementation beneath existing structures or naturally induced cementation around piles, cementation can develop in soils that have previously undergone initial static shear. However, the joint effect of cementation and initial static shear stress on subsequent cyclic loading behaviour remains largely uninvestigated, despite its crucial importance for understanding foundation response to seismic events and cyclic loading conditions. This study investigates the combined effects of cementation and initial static shear stress on the subsequent cyclic behaviour of granular soils using the discrete element method (DEM). First, DEM specimens with varying levels of cementation are subjected to undrained cyclic loading under different cyclic stress ratios (CSR) without initial static shear stress and the results align well with experimental results reported in the literature. Then, the role of initial static shear stress on the undrained cyclic response of the specimens is investigated. The results indicate that the liquefaction resistance of cemented soil depends on both CSR and initial static shear stress. The effect of initial static shear stress, which can be either beneficial or detrimental, is more pronounced at low CSR values. The DEM model developed in this study quantitatively captures actual cementation levels, offering practical guidance for engineering applications such as vibratory extraction of aged piles. Micromechanical analysis reveals that cementation helps maintain structural stability by preventing contact loss between particles, while initial static shear stress accelerates contact degradation and reduces structural stability during cyclic loading. These insights contribute to the development of multiscale constitutive models for cemented soils under cyclic loading conditions.

Keywords: Cemented granular soil, Cyclic loading, Initial shear, DEM

1 Introduction

Soils subjected to cyclic loads are commonly encountered in scenarios ranging from seismic events (e.g. earthquakes) and traffic-induced vibrations on road embankments to the operational conditions of offshore wind turbine pile foundations. The response of soil under such cyclic loading conditions is characterised by complex mechanisms involving progressive accumulation of plastic strains, changes in soil fabric, and potential development of excess pore water pressures [18, 32, 41]. It is possible to trigger soil liquefaction under cyclic loading and hence pose damage to surrounding infrastructures. A fundamental understanding of the cyclic behaviour and liquefaction resistance of soils is important for developing soil-predicting models, mitigating failure risks for structures such as offshore wind turbines (OWTs) [17, 19], and promoting the installation of OWTs by vibratory driving.

Extensive studies have been conducted to build a fundamental understanding of the soil behaviour subjected to cyclic loading. These works primarily involve the investigation of isotropically consolidated specimens under

symmetrical loading in compression and extension [28, 36]. Although this loading condition represents practical scenarios such as the free-field level ground under earthquakes [42], it is not applicable to conditions such as soils beneath a structure (Fig. 1) or in a sloping ground [41, 44], where soils may have undergone initial static shear before the cyclic loading. In this context, the cyclic behaviour of soils with the presence of initial static shear stress has been evaluated [22, 30, 35, 41, 42, 44]. These results highlight the important role of the initial static shear stress, in addition to the initial packing density and effective confining pressure, on the cyclic behaviour and liquefaction resistance of soils. For instance, Harder and Boulanger [9] reported that the effect of initial static shear stress is beneficial to liquefaction resistance for dense sand but is detrimental to loose sand. Yang and Sze [41] found that it is beneficial to the liquefaction resistance of loose sand at low levels of initial static shear stress, while it becomes detrimental at high levels.

Besides experimental tests, numerical approaches, particularly the discrete element method (DEM), have been adopted to evaluate the complex soil response under a wide range of conditions, offering insights that are not accessible from experimental observations [7, 10, 12, 37]. For instance, DEM was used to investigate the cyclic responses of sands with different properties, such as inherently anisotropic sands [38], samples with different fabric anisotropy [49], consolidation state [43] and initial static shear stress [52]. In addition, the effects of various test conditions, including the confining pressure [33] and cyclic and static stress ratios [13], were also reported, indicating that DEM is a powerful tool for investigating the cyclic behaviour of granular soils.

To mitigate the potential soil liquefaction due to seismic events, soils need to be reinforced through a process usually referred to as ground improvement. Among various ground improvement methods, non-invasive methods, which have minimal disturbance to the surrounding environment, are preferable for treating soils beneath structures. A typical non-invasive method is microbially induced carbonate precipitation (MICP) [21, 40, 50], it involves injecting a cementation solution (containing calcium chloride and urea) along with a bacterial solution, utilising natural bio-mineralisation processes to drive carbonate precipitation, thereby cementing the soil without altering the in-situ stress state. In such a scene, it is possible that the cementation is introduced on soil which has undergone initial static shear. In addition to artificially introduced cementation, as shown in Fig. 1, initial static shear stress can be applied on the soil around the pile shaft during pile installation [8]. During the operational time, natural cementation (e.g. calcite) can precipitate around the pile foundation [2, 5], an effect called soil ageing. Meanwhile, the soil surrounding the pile is subjected to cyclic loading from the dynamic forces of OWT, which interact with both the initial static shear stress and cementation. Consequently, the initial static shear stress and the precipitated natural cementation have a joint impact on the operational performance of OWTs. Moreover, at the end of an OWT's lifetime, the vibro-extraction method can be employed for pile removal, where inducing soil liquefaction can facilitate pile extraction [23]. Therefore, understanding the cyclic behaviour of cemented soil with the presence of initial static shear stress is important for optimising ground improvement strategies, ensuring the long-term serviceability of OWTs and promoting their extraction through vibro-extraction at the end of the pile lifetime.

Despite the crucial importance of understanding the cyclic response of cemented soils with the presence of initial static shear stress, knowledge gaps exist in this area: current research primarily focuses on the individual effects of either cementation or initial static shear stress on the cyclic behaviour of soil. For instance, Zhang et al. [51] employed DEM to investigate the cyclic liquefaction behaviour of cemented sand, with all the specimens being in an isotropic stress state prior to cyclic loading. Pan and Yang [22] and Wei and Yang [35] conducted experiments to examine the effect of initial static shear on the cyclic resistance of sands. However, the joint effect of cementation and initial static shear stress has not been comprehensively investigated through experimental studies or numerical simulations. Specifically, it remains unclear how much cementation should be introduced to achieve desirable liquefaction resistance under varying initial static shear conditions for liquefaction mitigation purposes, or conversely, how much effort should be applied to trigger liquefaction to facilitate the extraction of aged piles. Furthermore, during cyclic loading, it is challenging in experiments to access and monitor the evolution of microstructural properties that govern the macroscopic response of cemented soils. These knowledge gaps limit our ability to optimise ground improvement strategies and predict the long-term performance of foundations subjected to both cementation and initial shear stress. Therefore, this study aims to:

- Develop a comprehensive DEM framework to investigate the combined effects of cementation, initial static shear stress (SSR), and cyclic loading on granular soil behaviour.
- Quantify and establish the relationship between liquefaction resistance and cementation levels under different initial static shear conditions.
- Quantify microstructure evolution during cyclic loading to provide insights into the underlying mechanisms governing the macroscopic response.

This study is organised as follows: details of DEM simulations are given in Section 2. The simulation results in terms of the macroscopic cyclic response and microscopic insights are presented and discussed in Section 3 and Section 4, respectively. Section 5 summarises the main conclusions of this study.

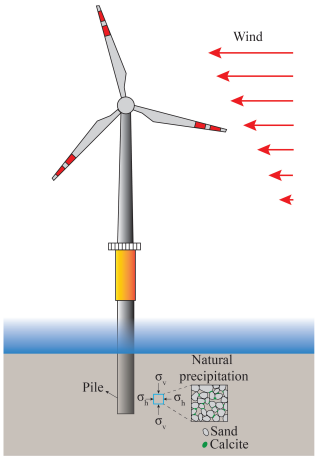

Fig. 1 Schematic illustration demonstrating that cementation is introduced into the soil element that has already undergone initial static shear: natural cementation precipitated in the soil around the OWT foundation.

2 DEM simulations

In this section, the adopted inter-particle contact law is introduced, followed by the procedure of generating DEM samples and the introduction of the undrained cyclic loading scheme.

2.1 Contact model

The DEM platform used in this study is YADE [31]. A cohesive-frictional contact model accounting for rolling and twisting resistance is used. Details of this contact model can be found in YADE documentation [31] and Zhang and Dieudonné [47]. For the sake of clarity, the contact law is also introduced below.

The normal force $\vec{F}_n$, incremental shear force $\Delta\vec{F}_s$, incremental rolling moment $\Delta\vec{M}_r$ and incremental twisting moment $\Delta\vec{M}_{tw}$ are calculated as:

$$\vec{F}_n = k_n u_n \vec{n} \tag{1}$$

$$\Delta\vec{F}_s = -k_s \Delta\vec{u}_s \tag{2}$$

$$\Delta\vec{M}_r = -k_r \Delta\vec{\theta}_r \tag{3}$$

$$\Delta\vec{M}_{tw} = -k_{tw} \Delta\vec{\theta}_{tw} \tag{4}$$

where u_n is the relative normal displacement of the two spheres, $\vec{n}$ is the normal contact vector, $\Delta\vec{u}_s$ is the incremental tangential displacement, and $\Delta\vec{\theta}_r$ and $\Delta\vec{\theta}_{tw}$ are the relative rotations due to rolling and twisting, respectively. k_n, k_s, k_r and k_{tw} are the contact normal stiffness, tangential stiffness, rolling stiffness and twisting stiffness, respectively, which are given by:

$$k_n = \frac{2E_1R_1E_2R_2}{E_1R_1 + E_2R_2} \tag{5}$$

$$k_s = \nu k_n \tag{6}$$

$$k_r = \alpha_r R_1 R_2 k_s \tag{7}$$

$$k_{tw} = \alpha_{tw} R_1 R_2 k_s \tag{8}$$

where R_1 and R_2, E_1 and E_2 are the radii, moduli of elasticity of the spheres, ν is the shearing stiffness coefficient, and α_r and α_{tw} are the rolling and twisting stiffness coefficients, respectively.

The normal, shear, rolling and twisting resistances are determined by:

$$F_n^{max} = \sigma_{S-C} \cdot S_c = \sigma_{coh} \cdot \min(R_1^2, R_2^2) \tag{9}$$

$$F_s^{max} = ||\vec{F}_n|| \tan\varphi_c' + \sigma_{S-C} \cdot S_c = ||\vec{F}_n|| \tan\varphi_c' + \sigma_{coh} \cdot \min(R_1^2, R_2^2) \tag{10}$$

$$M_r^{max} = ||\vec{F}_n||\eta_r \cdot \min(R_1, R_2) \quad (11)$$

$$M_{tw}^{max} = ||\vec{F}_n||\eta_{tw} \cdot \min(R_1, R_2) \quad (12)$$

where φ_c' is the contact friction angle, and η_r and η_{tw} are the resistance coefficients of rolling and twisting, respectively. σ_{S-C} is the cohesive strength depending on the intrinsic strength of the cement material and its adhesion at the grain surface [4]. S_c is the mean cohesive contact surface area [25]. In this study, the term $\sigma_{S-C} \cdot S_c$ is represented by $\sigma_{coh} \cdot \min(R_1, R_2)^2$, and hence different cementation amounts can be represented by varying σ_{coh}. σ_{coh} used in this study ranges from 0 to 200 kPa. These values can be linked to the actual $CaCO_3$ contents. According to Sarkis et al. [25], σ_{S-C} ranges from 2.75 MPa to 6.6 MPa. Using the relationship $S_c = \frac{\sigma_{coh} \cdot R_{mean}^2}{\sigma_{S-C}}$ with the mean grain radius R_{mean} = 2.18 mm, it yields an average S_c of 61205 μm^2, 122410 μm^2 and 244820 μm^2 for σ_{coh} = 50 kPa, 100 kPa and 200 kPa, respectively. Referring to the data provided by Sarkis et al. [25], in which S_c of 3326 μm^2, 4503 μm^2 and 7148 μm^2 correpsonds to a volume fraction of calcite of 1.9%, 6.2% and 8.8%, respectively. It should be noted that D_{50} of this study is 20 times larger than that of Sarkis et al. [25]. Consequently, assuming that calcite and silica have the same density, σ_{coh}=50kPa corresponds to an estimated calcite mass fraction of 1.5% (light cementation), σ_{coh}=100kPa to 6.5% (medium cementation), and σ_{coh}=200kPa corresponds to over 15% (high cementation). A further validation of σ_{coh} and its corresponding $CaCO_3$ content is presented in Section 3.2. The DEM parameters are listed in Table 2.

2.2 Sample preparation and model parameters

The preparation of DEM samples with different levels of initial static shear stress is illustrated in Fig. 2(a), which consists of the following two steps.

i. Isotropic compression. In this step, a sand packing containing 7000 sand particles is generated. All the particles are randomly located inside a 7 cm × 7 cm × 14 cm box formed by six rigid walls. There is no contact between the particles at this stage. The radius expansion method is used for isotropic compression, during which the radii of the sand particles are increased until the packing reaches a confining pressure of 50 kPa. The radius expansion is then turned off to fix the size of the particles (shown in Fig. 3), and the inter-particle friction angle is adjusted to reach a target porosity of 0.44. During this process, the rigid walls are controlled by a servomechanism to maintain the confining pressure. Once the target porosity is reached, the friction angle is set to the value used for the drained triaxial compression stage. After that, the isotropic compression is continued by moving the walls (instead of through radii expansion) until the mean effective stress (p'), or equivalently the lateral confining pressure (σ_h'), reaches the target value. The set of target values (σ_{h0}'), ranging from 85 kPa to 100 kPa, is listed in Table 1. The width of the sample (7 cm) is 14 times the mean grain diameter (D_{50}), satisfying the size of a representative volume element (RVE) suggested by Gu et al. [6] and Schmidt et al. [27].

ii. Drained triaxial compression. The consolidated samples are subjected to drained triaxial compression. In this process, the lateral confining pressure remains constant at σ_{h0}', while the vertical stress (σ_v') increases. The loading is terminated when p' reaches 100 kPa (see Fig. 2(a)). From the above steps, the sand samples subjected to different degrees of initial static shear are obtained. The degree of initial static shear can be described by the static stress ratio (SSR), which is the ratio of the static deviatoric stress (q_s) at the end of the drained triaxial compression to the mean effective stress (p_0') as indicated in Fig. 2, $SSR = \frac{q_s}{2p_0'}$, with $q_s = \sigma_{v0}'$ - σ_{h0}', where σ_{v0}' is the effective stress along the vertical direction (loading direction) at the end of the drained triaxial compression. The information of initial static shear stress on each sample is summarised in Table 1. After that, the cementation is introduced at grain contacts for building cemented samples by activating the contact cohesion (see Section 2.1). It should be noted that cementation in the soil matrix can exhibit several distribution patterns, such as at contact points, filling particle gaps, or on particle surfaces [3, 16, 48]. In this study, it is assumed that the cementation is distributed at contact points of sand grains, which is a widely used approach for simulating cemented soils using DEM [11, 15, 29].

2.3 Undrained cyclic loading scheme

The uncemented samples and cemented samples are subjected to undrained cyclic loadings. The cyclic loading is applied by moving the top wall at a constant velocity, while the four lateral walls are controlled to move correspondingly to keep the sample volume constant to mimic the undrained condition. The bottom wall is fixed. The moving direction of the top wall reverses as long as the deviatoric stress (q) reaches the predefined maximum or minimum value, *i.e.* $q_s \pm q_{Amp}$, as illustrated in Fig. 2(b), where q_{Amp} is the applied deviatoric stress amplitude. The cyclic amplitude can also be described by the cyclic stress ratio (CSR), defined as $CSR = \frac{q_{Amp}}{2p_0'}$. During the undrained cyclic loading, the deviatoric stress (q), mean effective stress (p') and pore pressure

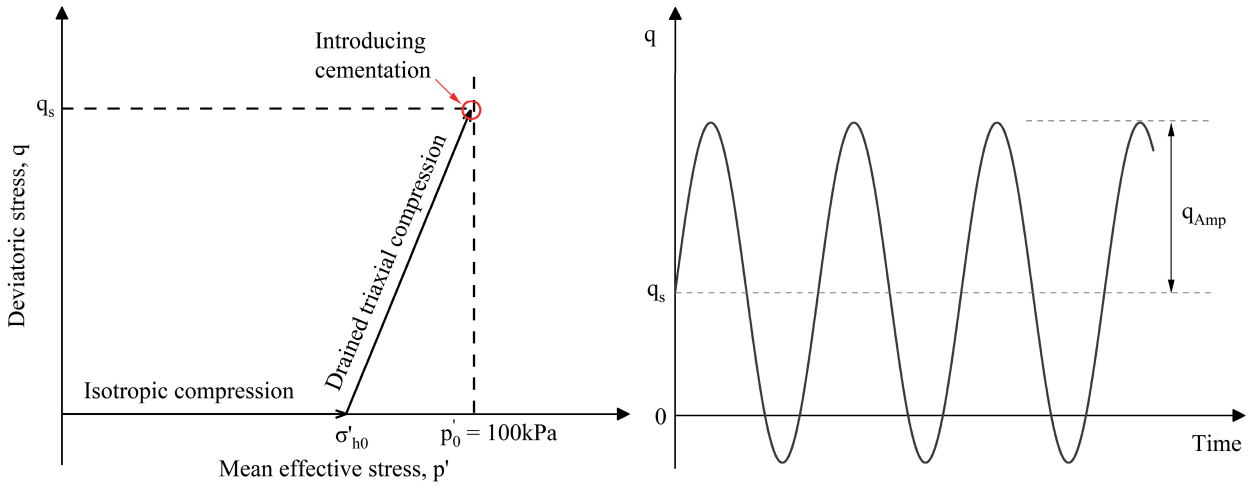

Fig. 2 Illustration of (a) the initial static shear process and (b) cyclic loading condition.

Table 1 Summarised information of DEM samples subjected to various test conditions. Unit: kPa for σ_{coh}, σ'_{v0}, σ'_{h0}, q_s and q_{Amp}.

Cementation (σ_{coh})	σ'_{v0}	σ'_{h0}	q_s	SSR	CSR
0	100	100	0	0	0.25, 0.28, 0.3, 0.33, 0.35
50	100	100	0	0	0.3, 0.35, 0.5
100	100	100	0	0	0.3, 0.33, 0.35, 0.38, 0.4, 0.5
200	100	100	0	0	0.3, 0.35, 0.4, 0.43, 0.44, 0.45, 0.5
0	106.66	96.66	10	0.05	0.25, 0.28, 0.3, 0.33, 0.35
50	106.66	96.66	10	0.05	0.3, 0.33, 0.35, 0.5
100	106.66	96.66	10	0.05	0.3, 0.33, 0.35, 0.38, 0.4, 0.5
200	106.66	96.66	10	0.05	0.3, 0.35, 0.4, 0.43, 0.45, 0.5
0	113.33	93.33	20	0.1	0.25, 0.28, 0.3, 0.33, 0.35
50	113.33	93.33	20	0.1	0.3, 0.33, 0.35, 0.5
100	113.33	93.33	20	0.1	0.3, 0.33, 0.35, 0.5
200	113.33	93.33	20	0.1	0.3, 0.35, 0.4, 0.43, 0.45, 0.47, 0.5
0	120	90	30	0.15	0.21, 0.25, 0.28, 0.3, 0.33, 0.35
50	120	90	30	0.15	0.3, 0.33, 0.35, 0.5
100	120	90	30	0.15	0.25, 0.3, 0.33, 0.35, 0.5
200	120	90	30	0.15	0.3, 0.35, 0.4, 0.5
0	130	85	45	0.225	0.21, 0.25, 0.28, 0.3, 0.33, 0.35
50	130	85	45	0.225	0.3, 0.33, 0.35, 0.5
100	130	85	45	0.225	0.23, 0.25, 0.3, 0.33, 0.35, 0.5
200	130	85	45	0.225	0.3, 0.35, 0.4, 0.5

(u) are defined as: $q = \sigma'_v - \sigma'_h$, $p' = (\sigma'_v + 2\sigma'_h)/3$, $u = p'_0 - p'$, respectively [7]. During the simulation, the unbalanced force, which is defined as the ratio of mean summary force on bodies and mean force magnitude on interactions, is below 5×10^{-4} for ensuring a quasi-static loading condition [31].

3 Macroscopic mechanical behaviour

In this section, the undrained cyclic triaxial response of cemented samples with different cementation levels, CSR and SSR are investigated. The simulation results of the uncemented samples are also presented for comparison. Since this study focuses on the pre-liquefaction behaviour and liquefaction resistance of cemented sands, the cyclic loading is terminated when the samples reach their liquefaction states.

3.1 Undrained cyclic response

Fig. 4 presents the undrained cyclic responses of uncemented samples with various levels of initial static shear stress. For the sample with SSR=0, as shown in Fig. 4(a), it is subjected to symmetrical cyclic deviatoric stress. During the cyclic loading, the pore pressure is built up gradually. Meanwhile, the effective stress is continuously decreased. After around 10 cycles, the pore pressure increases abruptly, and the mean stress decreases rapidly. Eventually, the pore pressure builds up to 100 kPa, and the deviatoric stress and the mean effective stress reduce

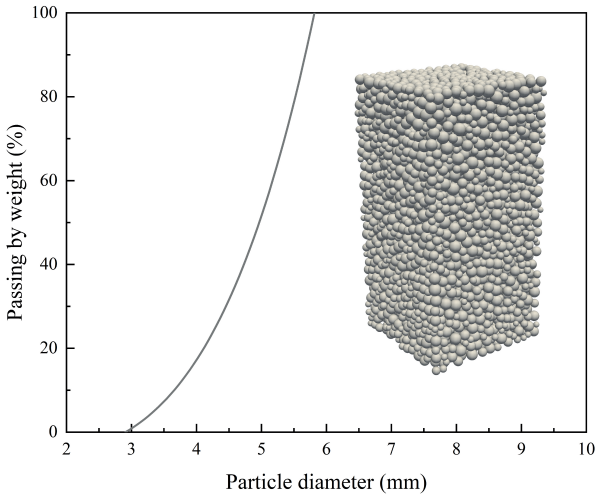

Fig. 3 Particle size distribution of the DEM sample. $D_{50} = 4.97$ mm.

Table 2 Properties of particles used in the DEM simulations.

Properties	Symbol	Unit	Value
Density	ρ	kg/m^3	2650
Young's modulus	E	MPa	200
Shearing stiffness coefficient	ν	-	0.3
Friction angle	φ_c'	$^\circ$	19
Rolling stiffness coefficient	α_{r}	-	0.8
Twisting stiffness coefficient	α_{tw}	-	0.8
Rolling resistance coefficient	η_{r}	-	0.15
Twisting resistance coefficient	η_{tw}	-	0.15
Cohesive strength	σ_{coh}	kPa	50, 100, 200

to zero, indicating the onset of liquefaction. A flow-type failure mode can be identified for this sample, as the strain developed slightly at the beginning, while a significant deformation occurs just before liquefaction.

The cyclic responses of uncemented samples with the presence of initial shear stress are shown in Fig. 4(b), (c) and (d). The samples undergo asymmetric cyclic loading in these cases. For the uncemented sample with a low SSR, as shown in Fig. 4(b), its cyclic behaviour and failure mode are similar to those not experiencing initial static shear. It is worth noting that it shows a slight increase (from 12 to 13) in the number of cycles to liquefaction. Comparing Figs. 4(c) and (d) to (a), it can be found that as the level of initial static shear stress (SSR) increases, the pore pressure builds up more rapidly during the first two cycles, and a lower number of cycles is needed to trigger the liquefaction. Namely, the presence of a light initial static shear stress is beneficial to liquefaction resistance. However, as SSR increases, the presence of initial static shear stress tends to reduce the liquefaction resistance. This finding aligns with that reported in Harder and Boulanger [9], as also pointed out in Yang and Sze [41]. They reported that the effect of initial static shear stress is negative for loose sand under the condition that the effective confining pressure is less than about 300 kPa and SSR is below 0.3. Yang and Sze [41] and Yang and Pan [44] further established the effect of SSR and reported that the presence of initial static shear stress is beneficial to the liquefaction resistance of loose sand at a low level of the initial shear stress, but it becomes detrimental at high SSR levels. A critical SSR of 0.1 was reported by Yang and Pan [44]. The simulation conditions presented in Fig. 4 fall within the conditions Yang and Pan [44] outlined. Moreover, the presence of initial static shear stress changes the failure mode. It can be observed from the stress-strain relationship in Fig. 4(c) that the strain develops gradually and only occurs in one direction, which is characterised as cyclic mobility. As SSR increases, such behaviour becomes more pronounced, as shown in Fig. 4(d).

Fig. 5 shows the undrained cyclic responses of cemented samples with $\sigma_{coh} = 100$ kPa. Apparently, the introduction of cementation greatly enhances the liquefaction resistance compared to the corresponding uncemented sample shown in Fig. 4, indicating that the effect of cementation on liquefaction resistance is always beneficial. For the cemented sample without initial static shear (i.e. SSR=0), as shown in Fig. 5(a), it takes around 52 cycles for the pore pressure to gradually build up to 10% of the initial mean effective stress. During this process, the mean effective stress progressively decreases, and the axial strain cyclically changes in a limited range. It is during the final several cycles that the pore pressure abruptly increases, leading to sample liquefaction. The introduction of cohesion does not change the failure mode, as a similar stress-strain response can be observed in

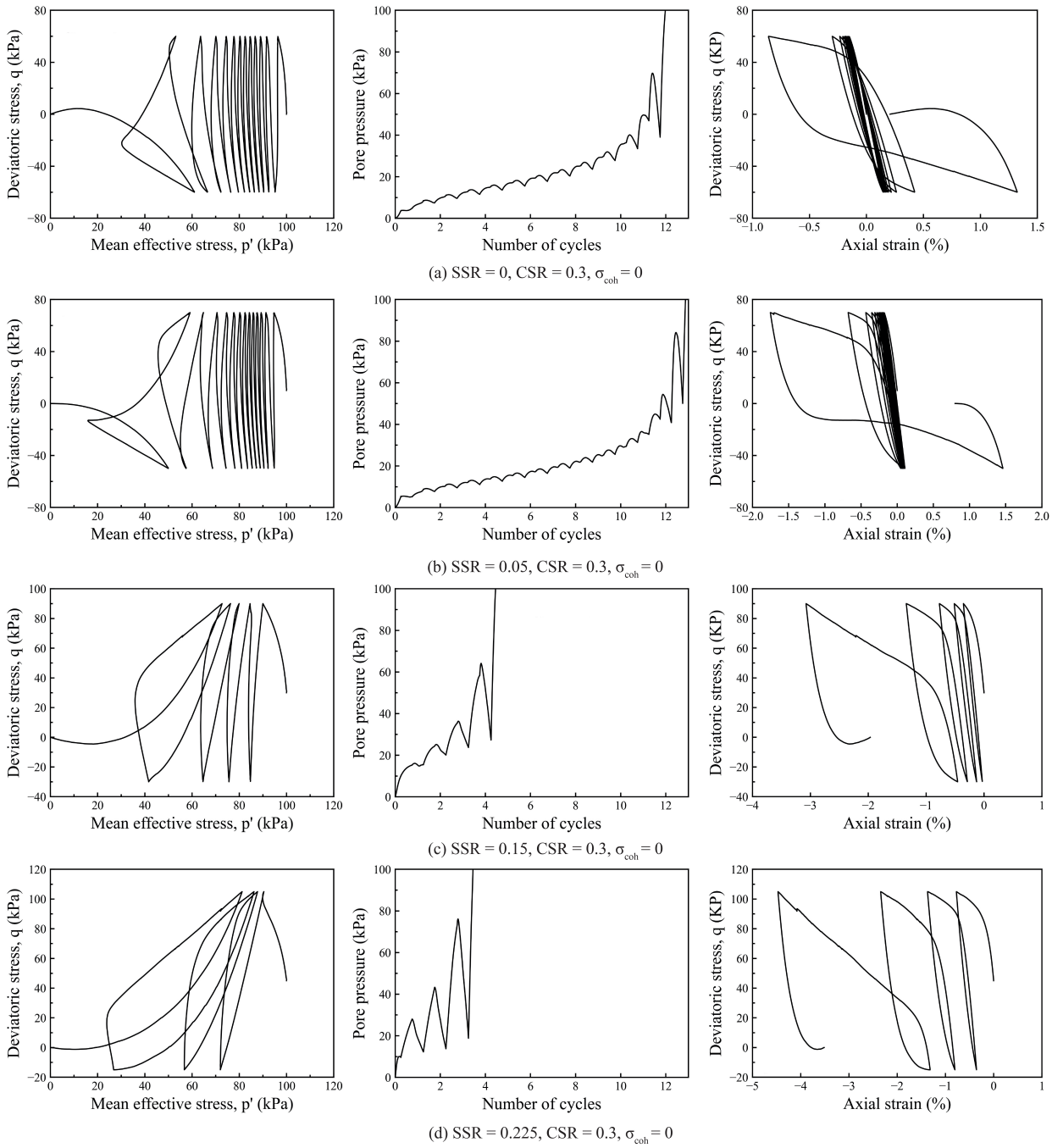

Fig. 4 Undrained cyclic response: (left) stress path, (middle) evolution of pore pressure with cyclic number and (right) evolution of deviatoric stress with axial strain of uncemented samples ($\sigma_{coh} = 0$) with CSR=0.3 and (a) SSR=0, (b) SSR=0.05, (c) SSR=0.15 and (d) SSR=0.225.

the corresponding uncemented sample shown in Fig. 4. For the cemented sample with a low SSR (SSR=0.05), an obvious enhancement in liquefaction resistance can be observed due to the combined beneficial effect of SSR and cementation. In contrast, a large decrease in the number to trigger liquefaction can be observed in Fig. 5(c) and (d) compared to Fig. 5(a), suggesting a large SSR is detrimental to the liquefaction resistance of cemented samples.

The undrained cyclic responses of cemented samples with a higher cementation level (σ_{coh} = 200 kPa) are presented in Fig. 6. The simulations terminate when the number of cycles reaches 140, at which point the sample is still far from liquefaction. For the case with SSR= 0, the mean effective stress almost remains constant, characterised as a vertical line in Fig. 6(a). Negligible pore pressure is developed during the cyclic loading. The stress-strain relationship shows as a straight line as well, with a maximum axial strain of 0.12%. This indicates a non-liquefiable state. For cemented samples with a higher SSR presented in Fig. 6, more pore pressure is built up, although it remains at a low value, in the first few cycles as SSR increases. Consequently, the mean effective

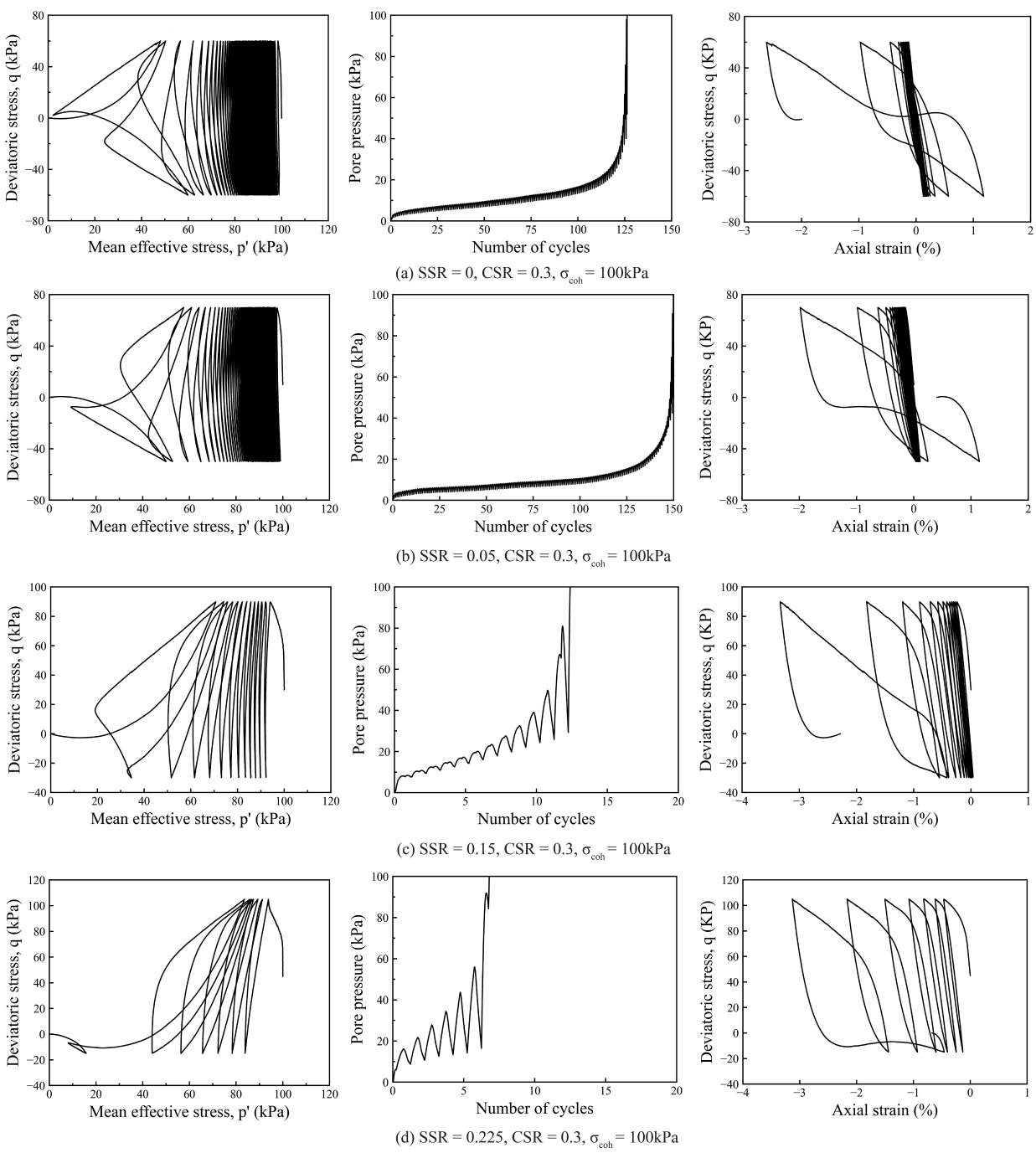

Fig. 5 Undrained cyclic response: (left) stress path, (middle) evolution of pore pressure with cyclic number and (right) evolution of deviatoric stress with axial strain of cemented samples (σ_{coh} = 100 kPa) with CSR=0.3 and (a) SSR=0, (b) SSR=0.05, (c) SSR=0.15 and (d) SSR=0.225.

stress reduces in the first few cycles. As cyclic loading progresses after the first few cycles, the pore pressure and the mean effective stress exhibit negligible change.

3.2 Liquefaction resistance

To demonstrate the effect of cementation on the liquefaction resistance, Fig. 7 plots the number of cycles upon liquefaction (N_f) of cemented samples under various CSR. Data obtained from experimental tests [39] are also included for comparison. Note that SSR = 0 for the samples presented in Fig. 7. It can be seen that the DEM results capture the effects of CSR and cementation reported from the literature. Specifically, a higher CSR leads to a lower N_f, indicating that liquefaction is easier to trigger under a high cyclic stress amplitude. The presence of cementation strengthens the resistance to liquefaction, and this resistance increases with the degree of cementation. In addition, the CSR-N_f relationship is fitted by a power-law empirical equation [39], which is

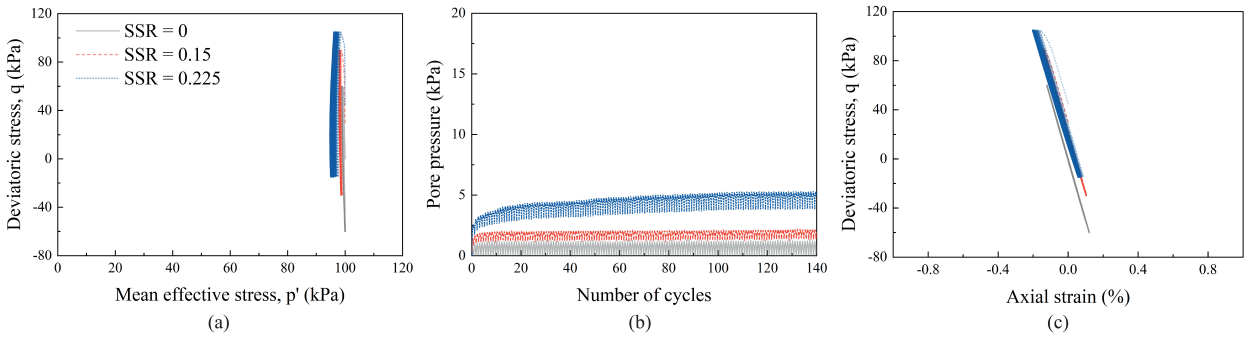

Fig. 6 Effect of SSR on the undrained cyclic response of cemented samples with σ_{coh} = 200 kPa and CSR=0.3: (a) stress path, (b) evolution of pore pressure with cyclic number and (c) evolution of deviatoric stress with axial strain.

described in Eq. (13).

$$CSR = aN_f^{-b} \tag{13}$$

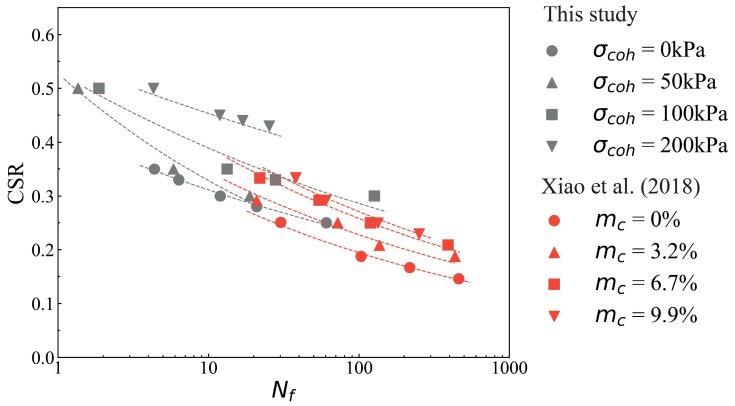

Fig. 7 Comparison of DEM results (this study) with experimental results on CSR-N_f relationship. m_c is the mass fraction of carbonate in Xiao et al. [39].

It can be seen that the DEM results align closely with the data from Xiao et al. [39], as evidenced by their overlapping trend lines. This also implies the studied range of σ_{coh} can represent practical cementation amounts observed in experiments, confirming the estimation in Section 2.1. This agreement between numerical simulations and laboratory experiments validates the presented modelling approach, demonstrating that the developed DEM model enables not only phenomenological investigation of cementation effects but also quantitative assessment of how different cementation levels influence the liquefaction behaviour.

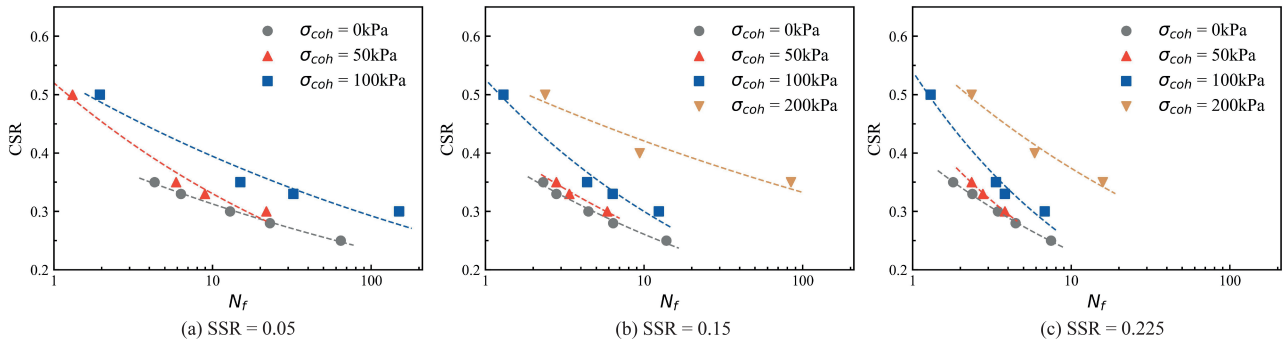

Fig. 8 Effect of cementation on the number of cycles to trigger liquefaction (N_f): (a) SSR=0.05; (b) SSR=0.15 and (c) SSR=0.225.

The combined effect of cementation and SSR on the liquefaction resistance is shown in Fig. 8. The effect of cementation on samples with the presence of initial static shear stress is identical to what is observed in samples with SSR=0 (Fig. 7), though it's worth noting that the CSR-N_f trend line becomes steeper as SSR increases, suggesting a decrease in liquefaction resistance under a high SSR value.

To quantify the effect of cementation and SSR on cyclic resistance, all data are fitted using Eq. (13). The fitted parameters, namely, a, b in Eq. (13), are summarised in Table 3. The parameter a indicates the CSR that leads to liquefaction in a single cycle (N_f=1), thus a higher value of a suggests a higher liquefaction resistance. The parameter b describes the change rate of CSR with increasing number of cycles. The correlations between parameters a and b with cementation content (m_c) and SSR are plotted in Fig. 9. It can be seen from Fig. 9(a) that parameter a shows a linear relationship with m_c, while SSR has minimal influence on this relationship. Fig. 9(b) indicates that parameter a is independent of SSR. Parameter b is affected by both cementation content and SSR as shown in Fig. 9(c) and (d), where parameter b exhibits a quadratic relationship with m_c, and an exponential relationship with SSR. Based on these observations, Eq. (14) and Eq. (15) are proposed as follows.

$$a = k_1 m_c + k_0 \tag{14}$$

$$b = (k_2 m_c^2 + k_3 m_c + k_4) \times e^{k_5 SSR} \tag{15}$$

where a and b are the parameters in Eq. 13, k_i (i = 0 - 5) are fitted parameters. m_c is the mass fraction of cementation and SSR is the initial static shear stress. By integrating Eq. (14) and Eq. (15) into Eq. (13), the soil liquefaction resistance described by the number of cycles to liquefaction (N_f) is established as a function of CSR, SSR and m_c.

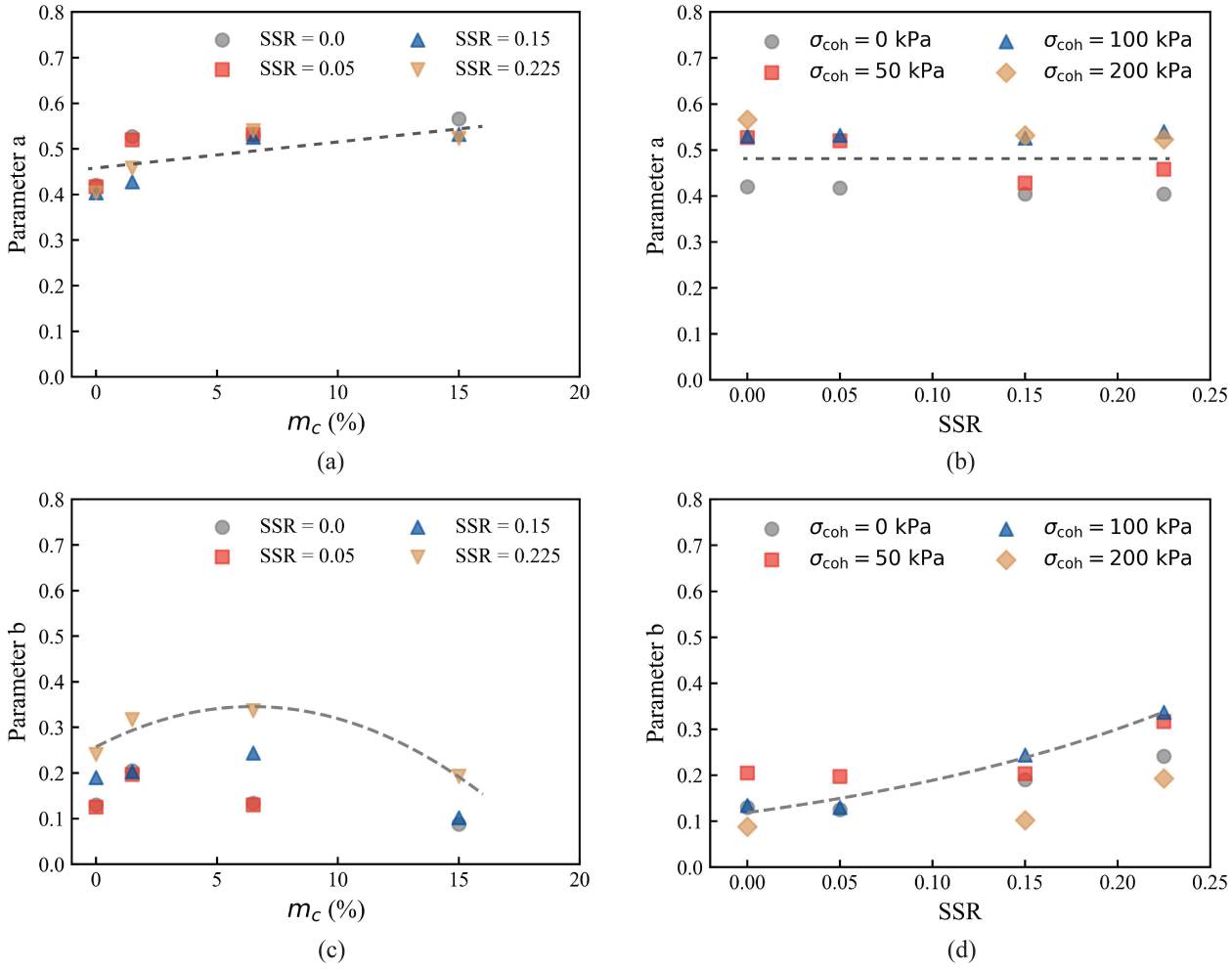

Fig. 9 Correlation between parameter a and b of Eq. (13) with carbonate content (m_c) and SSR, respectively. The dashed line is the trending line.

Fig. 10(a) shows the effect of initial static shear stress (SSR) on the liquefaction resistance of cemented samples. All the samples presented in Fig. 10 have the same σ_{coh} of 100 kPa. The effect of SSR, either beneficial or detrimental, can thus be easily identified in Fig. 10(a). Using the case of SSR=0 as a reference, the curve shifts to the right for the case of SSR=0.05, indicating an increase in N_f. As SSR increases, the curves shift to the left side, suggesting the detrimental effect increases as SSR increases. Furthermore, the magnitude of the

Table 3 Summarisation of the fitted parameters. R^2: coefficient of determination.

SSR	σ_{coh} (kPa)	a	b	R^2
0	0	0.420	0.130	0.992
	50	0.527	0.205	0.980
	100	0.530	0.134	0.942
	200	0.566	0.088	0.982
0.05	0	0.417	0.125	0.996
	50	0.520	0.197	0.972
	100	0.532	0.130	0.944
0.15	0	0.404	0.190	0.986
	50	0.428	0.203	0.979
	100	0.526	0.244	0.975
	200	0.532	0.102	0.927
0.225	0	0.404	0.241	0.998
	50	0.458	0.317	0.998
	100	0.540	0.337	0.975
	200	0.523	0.193	0.975

effect of SSR depends on CSR, which is highlighted in Fig. 10(b). To demonstrate the change in liquefaction resistance, N_f is normalised which is defined as $\frac{N_f^{SSR=0}-N_f}{N_f^{SSR=0}}$, where $N_f^{SSR=0}$ represents the N_f for the sample without initial static shear stress and N_f for the case with SSR = 0.05, 0.15 or 0.225. Thus, a positive normalised N_f represents a detrimental effect and the higher the value, the more significant the detrimental effect, as shown in Fig. 10(b). While a negative normalised N_f represents a beneficial effect. It can be seen in Fig. 10(b) that both the beneficial and detrimental effects are more pronounced at a low CSR, and they decrease linearly as CSR increases.

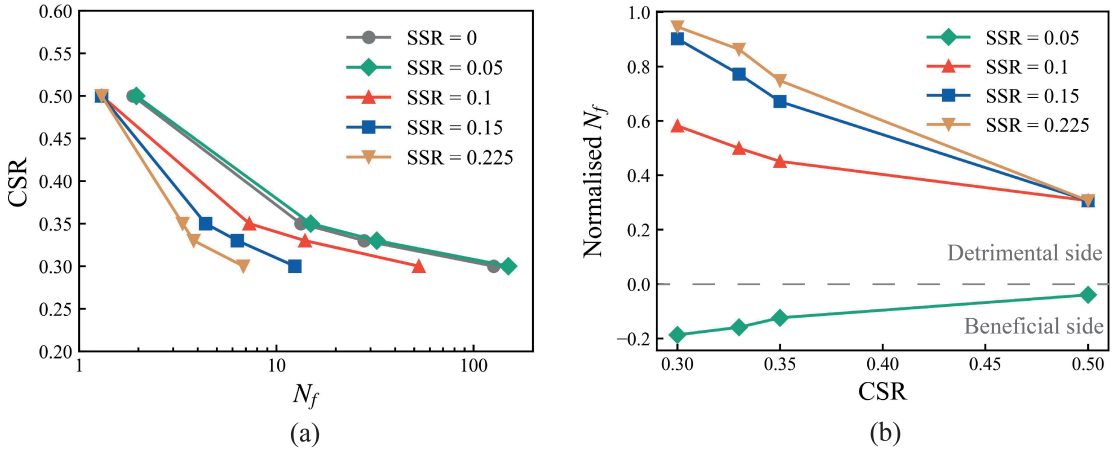

Fig. 10 (a) Effect of initial static shear stress (SSR) on the number of cycles to trigger liquefaction (N_f); (b) Evolution of normalised N_f with CSR. σ_{coh}=100 kPa for samples presented herein.

The combined effect of CSR, SSR and cementation on the cyclic resistance is further elaborated in Fig. 11. In Fig. 11, each symbol represents a single simulation in which liquefaction either occurs or does not within a given number of cycles (N_f^*). The two areas, namely, the liquefaction zone and the not-yet liquefied zone, can thus be estimated. It is clear to see that the not-yet-liquefied zone gradually increases as cementation content increases. This figure is a supplement to Fig. 8 and Fig. 10, which show the number of cycles to liquefaction (N_f). In engineering scenarios such as the extraction of aged piles (cementation may present [5]) by the vibratory method, it is also good to know the number of cycles needed to trigger liquefaction. Such information can then be inferred from the diagram shown in Fig. 11.

3.3 Bond breakage behaviour

The effect of σ_{coh}, SSR and CSR on bond breakage behaviour is illustrated in Figs. 12(a), (b) and (c), respectively. The bond breakage ratio, defined as the ratio of the number of broken bonds to the total number of bonds, is used to describe the bond breakage progress during cyclic loading. In general, a higher cementation leads to less bond breakage given the same number of cycles. Notably, bond breakage becomes negligible at

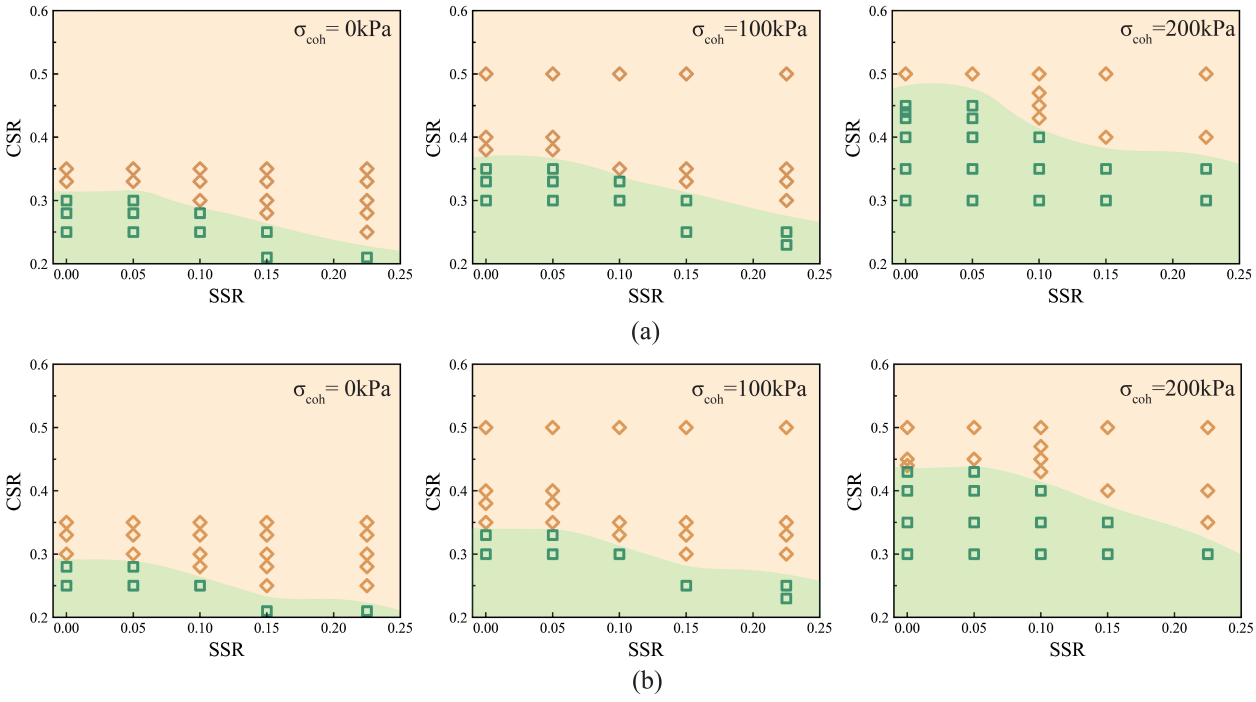

Fig. 11 Liquefaction status after a given number of cycles (N_f^*): (a) $N_f^* = 10$; (b) $N_f^* = 20$. The green square symbol represents not-yet-liquefied status, the yellow diamond symbol represents the liquefied status.

high cementation (σ_{coh}=200 kPa), corresponding to a non-liquefied state as shown in Fig. 6. Additionally, an increase in SSR (except SSR=0.05) or CSR can lead to a greater extent of bond breakage under the same cyclic loading conditions. It can also be inferred from Fig. 12 that the bond breakage behaviour exhibits a stepwise incremental pattern. Specifically, the breakage ratio increases during the first quarter of each cycle, followed by a plateau in the second quarter, it rises again in the third quarter and remains constant in the final quarter. Such an evolution pattern repeats in the following cycles until reaching the liquefaction state. Furthermore, a major breakage occurs during the first cycle. For instance, for the case with SSR=0.225, CSR=0.3 and σ_{coh}=100 kPa, 47% of bonds broken in the first cycle, occupying 59% of the total bond breakage ratio. Moreover, this breakage intensity in the first cycle is affected by σ_{coh}, SSR and CSR. A high σ_{coh} can significantly reduce the bond breakage in the first cycle, while a high SSR or CSR leads to more severe bond breakage in the first cycle.

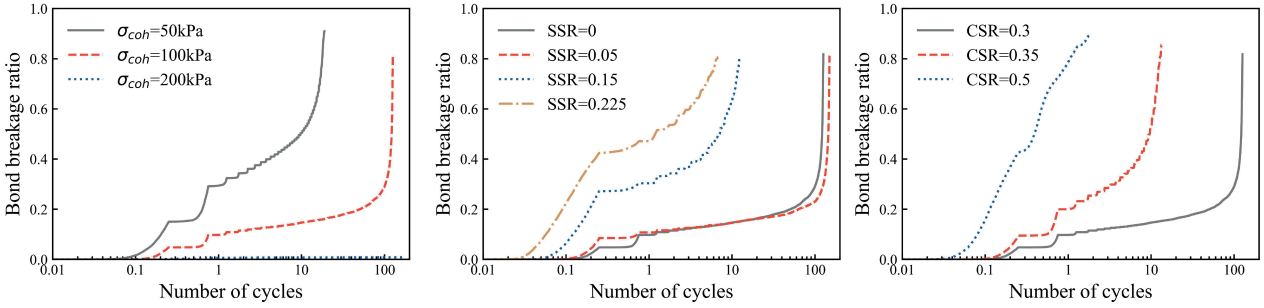

Fig. 12 Effect of (a) cementation level (σ_{coh}), (b) SSR and (c) CSR on the evolution of bond breakage ratio with the number of cycles.

Since a major breakage occurs in the first cycle, the density distribution of broken bonds at the end of the first cycle is presented to investigate the spatial distribution of the bond breakage behaviour. Fig. 13 compares the density distribution of broken bonds for cemented samples under different conditions. It can be observed that for the cemented sample with low cementation (Fig. 13(a)), bond breakage is uniformly distributed throughout the sample. In contrast, higher cementation results in a less uniform distribution of bond breakage (Fig. 13(b)). For other samples presented in Fig. 13, they demonstrate uniform breakage distribution, independent of the

change in SSR or CSR. This finding is in agreement with observations by Zhang et al. [51], in which a uniform bond breakage was observed in the DEM cemented sample.

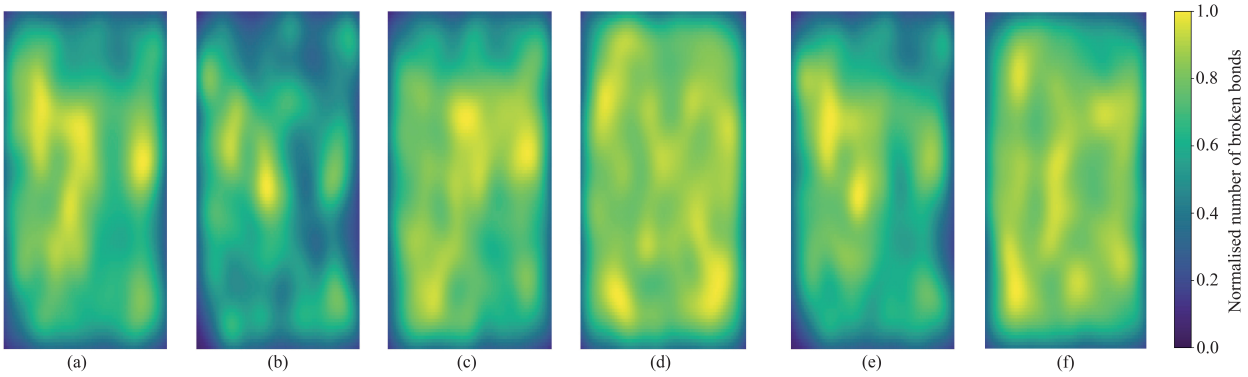

Fig. 13 Density distribution of broken bonds at the end of the 1st cycle, projection on X-Y plane: (a) SSR=0, CSR=0.3, σ_{coh}=50 kPa; (b) SSR=0, CSR=0.3, σ_{coh}=100 kPa; (c) SSR=0.15, CSR=0.3, σ_{coh}=100 kPa; (d) SSR=0.225, CSR=0.3, σ_{coh}=100 kPa; (e) SSR=0, CSR=0.35, σ_{coh}=100 kPa; (f) SSR=0, CSR=0.5, σ_{coh}=100 kPa.

4 Microstructural analysis

In this section, microscopic analysis is conducted, from the point of view of coordination number and fabric anisotropy, to understand the combined effect of cementation and initial static shear stress on the microstructural response of granular soils under cyclic loadings.

4.1 Coordination number

The coordination number (Z) characterises the average contacts per particle and has been widely used to describe the structural connectivity of granular materials [34, 47]. It is defined as:

$$Z = \frac{2N_c}{N_p} \tag{16}$$

where N_c is the number of inter-particle contacts, and N_p is the number of particles.

Fig. 14 compares the evolution of Z of samples with various σ_{coh} and subjected to different SSR and CSR during cyclic loading. For the sake of comparison, Z is plotted against the normalised cyclic number (N/N_f). In general, it can be observed that the coordination number gradually decreases as the cyclic loading progresses for all the samples, which eventually reach liquefaction. This implies a continuous loss of inter-particle contacts during cyclic loading. The coordination number drops to a value below 2 when the sample approaches the liquefaction state, suggesting an unstable structure upon liquefaction since an individual particle can not be stable given less than 2 contacts in a 3D granular system. The effect of σ_{coh} can be inferred from Fig. 14(a), a positive effect of cementation in preventing contact loss is evident. In addition, the introduction of initial static shear stress leads to a more severe loss in inter-particle contacts, and this detrimental effect is more pronounced at a higher SSR (Fig. 14(b)). The same trend is also observed in terms of the effect of CSR as shown in Fig. 14(c).

4.2 Fabric anisotropy

The macroscopic behaviour of granular material is not only associated with the average contact number but also the arrangement of the particles [14, 45, 55]. Such a property is often characterised by fabric tensors [1, 46, 53, 54]. In this study, the contact-normal-based fabric tensor [20, 26] is adopted to describe the fabric and hence quantify the fabric anisotropy. The fabric tensor ϕ_{ij} is calculated by:

$$\phi_{ij} = \frac{1}{N_c} \sum_{c=1}^{N_c} n_i^c n_j^c \tag{17}$$

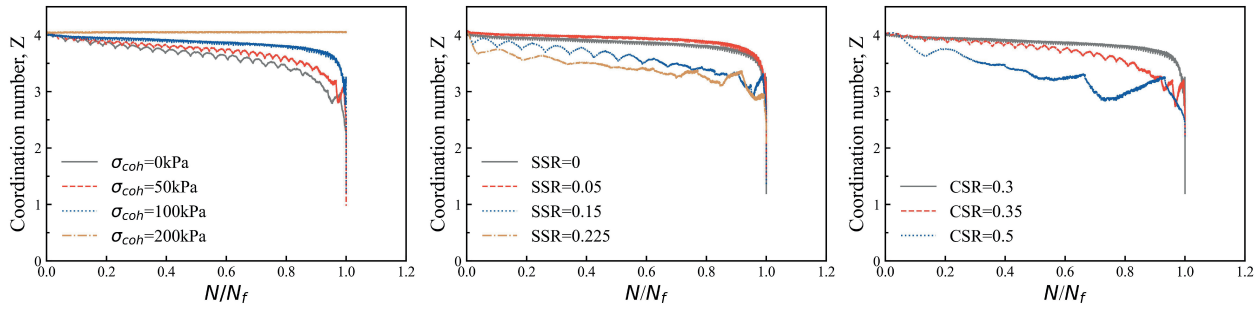

(a) SSR = 0, CSR = 0.3 (b) CSR = 0.3, σ_{coh} = 100kPa (c) SSR = 0, σ_{coh} = 100kPa

Fig. 14 Effect of (a) cementation level (σ_{coh}), (b) SSR and (c) CSR on the evolution of coordination number with the normalised number of cycles.

where N_c is the number of inter-particle contacts, and n^c is the unit contact normal vector. A scalar variable ϕ_d proposed by Barreto and O'Sullivan [1] is used to describe the fabric anisotropy (ϕ_d). It is defined as:

$$\phi_d = \frac{1}{\sqrt{2}}\left[(\phi_1-\phi_2)^2+(\phi_2-\phi_3)^2+(\phi_1-\phi_3)^2\right]^{1/2} \tag{18}$$

where ϕ_1, ϕ_2 and ϕ_3 are the principal values of the fabric tensor ϕ_{ij}. This definition of ϕ_d reduces to ϕ_1-ϕ_3 for axisymmetric conditions.

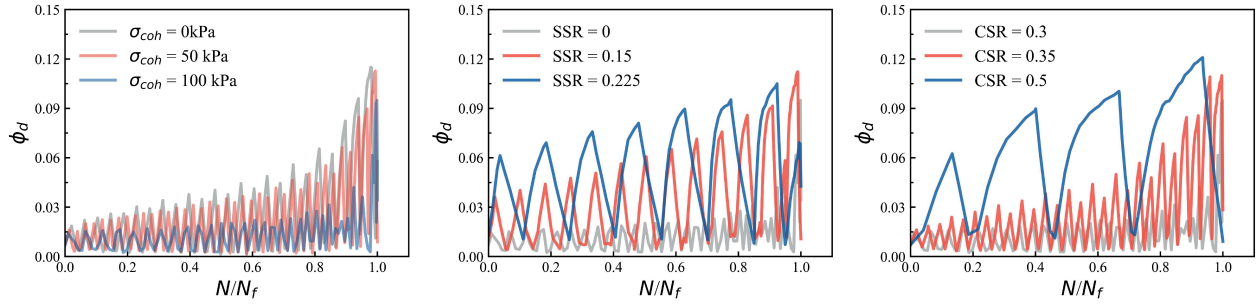

(a) SSR = 0, CSR = 0.3 (b) CSR = 0.3, σ_{coh} = 100kPa (c) SSR = 0, σ_{coh} = 100kPa

Fig. 15 Effect of (a) cementation level (σ_{coh}), (b) SSR and (c) CSR on the evolution of fabric anisotropy with the normalised number of cycles.

Fig. 15 presents the evolution of fabric anisotropy with the normalised number of cycles. All the samples demonstrate a low fabric anisotropy at the beginning of the cyclic loading, while it increases either gradually or abruptly when approaching the liquefaction state. For the uncemented sample without being subjected to initial static shear (Fig. 15(a)), ϕ_d increases gradually in a cyclic pattern. With the introduction of cementation, the variation of ϕ_d is constrained during the cyclic loading, and its evolution pattern transitions from a gradual mode to an abrupt mode as cementation increases. For samples subjected to initial static shear (Fig. 15(b)), ϕ_d increases in a gradual manner and exhibits a larger variation as SSR increases. Fig. 15(c) indicates that as CSR increases, the evolution of fabric anisotropy transitions to a more gradual pattern, with the magnitude of variation in fabric anisotropy also increasing. Consequently, the evolution of fabric anisotropy, including the variation magnitude and the development pattern, is affected by cementation level, SSR and CSR.

The fabric anisotropy of the soil skeleton is quantified by ϕ_d. Similarly, the fabric anisotropy of cementation (ϕ_d^c) can be derived by considering only the cemented contacts in Eq. (17). Fig. 16 presents the evolution of fabric anisotropy of cementation with the normalised number of cycles. In general, the cementation anisotropy shows an increasing trend with the number of cycles in all specimens. It can be seen that a higher cementation level results in consistently lower fabric anisotropy compared to a lower cementation, while increased SSR and CSR intensify fabric anisotropy throughout the loading process.

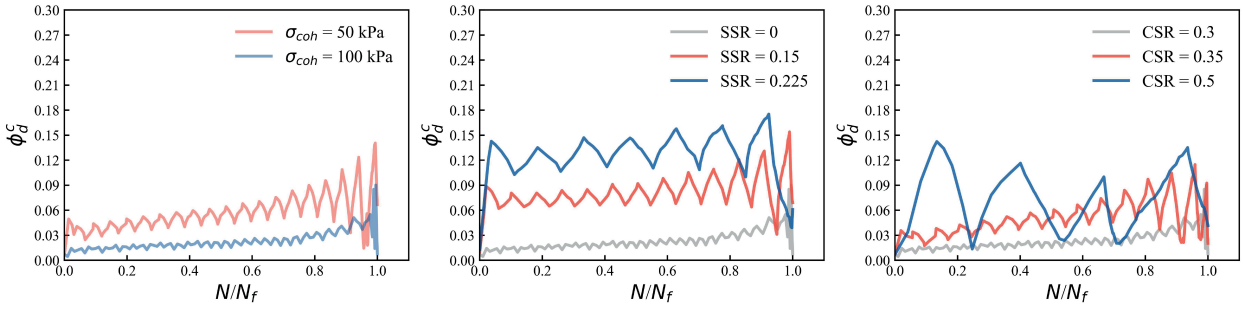

(a) SSR = 0, CSR = 0.3 (b) CSR = 0.3, σ_{coh} = 100kPa (c) SSR = 0, σ_{coh} = 100kPa

Fig. 16 Effect of (a) cementation level (σ_{coh}), (b) SSR and (c) CSR on the evolution of fabric anisotropy of cemented contacts with the normalised number of cycles.

5 Conclusions

In engineering scenarios where cementation develops in soils that have previously undergone initial static shear, both cementation and initial static shear stress jointly affect the soil behaviour on subsequent cyclic loading. However, their combined effect was insufficiently understood. Gaining insight into this interaction is essential for practical applications, such as non-invasive cementation treatments for soils beneath structures and the natural precipitation of cementation around offshore wind piles. To fill this knowledge gap, this study employs three-dimensional DEM to investigate the interplay between cementation and initial static shear stress. Cementation levels are systematically varied to represent realistic conditions ranging from light to heavy cementation. DEM specimens with different combinations of cementation and static shear stress ratio (SSR) are then subjected to undrained cyclic loading across a wide range of cyclic stress ratios (CSR). The major findings of this study are as follows:

- A low level of initial static shear stress has a beneficial effect on liquefaction resistance. However, as SSR increases, its effect becomes detrimental, aligning with the experimental findings reported in Yang and Sze [41] for uncemented sand.
- The introduction of cementation consistently enhances liquefaction resistance, regardless of the presence or magnitude of SSR. Moreover, the effectiveness of cementation increases with its level. The DEM results align well with experiments conducted without an initial SSR, allowing not only a phenomenological investigation of cementation effects but also a quantitative assessment of how varying cementation levels influence liquefaction behaviour.
- The liquefaction resistance of the cemented sample depends on both CSR and SSR. Notably, the effect of SSR, whether beneficial or detrimental, is more pronounced at a low CSR, and it decreases linearly as CSR increases.
- A new empirical equation is proposed to describe the relationship between the number of cycles to liquefaction (N_f) with CSR, cementation level and SSR. This equation extends the widely used form (CSR = aN_f^{-b}) by incorporating the combined effects of cementation level and SSR.
- Bond breakage in cemented specimens occurs in a stepwise pattern during cyclic loading, with significant breakage occurring in the first cycle. The extent of bond breakage is strongly influenced by cementation level, SSR, and CSR. While cementation mitigates bond breakage, increasing SSR or CSR intensifies it.
- Micromechanical analysis reveals that cementation helps maintain inter-particle contacts, contributing to a more stable soil structure under cyclic loading. In contrast, SSR promotes contact loss and reduces structural stability. Additionally, fabric anisotropy evolves during cyclic loading, with its magnitude and progression (gradual or abrupt) being affected by cementation level, SSR, and CSR.

This study provides valuable insights into the combined effects of cementation and initial static shear stress on the cyclic behaviour of soil. The findings provide practical guidance for engineering applications such as vibratory extraction of aged piles and contribute to the development of multiscale constitutive models for cemented soils under cyclic loading conditions. Future research is suggested to consider the effect of cementation homogeneity, as practical cementing processes often result in non-uniform distributions [21, 24] that may significantly influence liquefaction resistance and failure mechanisms.

Acknowledgements

This work was supported by the SAGE-SAND (Soil ageing around offshore wind turbine foundations - from operational response to decommissioning) project, funded by the Energy Transition Fund (ETF), Belgium and the NSFC-FNRS project (No. 52311530699, No. R.M008.23). Their support is gratefully acknowledged.

Data Availability

The data that support the findings of this study are available from the corresponding author upon reasonable request.

Declarations

Conflict of interest The authors declare no competing interests.

References

[1] Barreto D, O'Sullivan C (2012) The influence of inter-particle friction and the intermediate stress ratio on soil response under generalised stress conditions. Granul Matter 14(4):505–521

[2] Bittar E, Lehane B, Zheng H (2023) The role of physicochemical processes in aging of shaft friction of driven steel piles in sand. Can Geotech J 61(9):1873–1885

[3] Cheng L, Shahin MA, Mujah D (2016) Influence of key environmental conditions on microbially induced cementation for soil stabilization. J Geotech Geoenviron Eng 143(1):04016083

[4] Dadda A, Geindreau C, Emeriault F, et al (2019) Influence of the microstructural properties of biocemented sand on its mechanical behavior. Int J Numer Anal Methods Geomech 43(2):568–577

[5] Gavin K, Igoe D (2021) A field investigation into the mechanisms of pile ageing in sand. Géotechnique 71(2):120–131

[6] Gu X, Lu L, Qian J (2017) Discrete element modeling of the effect of particle size distribution on the small strain stiffness of granular soils. Particuology 32:21–29

[7] Gu X, Zhang J, Huang X (2020) DEM analysis of monotonic and cyclic behaviors of sand based on critical state soil mechanics framework. Comput Geotech 128:103787

[8] Guo N, Liu H, Li B, et al (2023) DEM study of the stress fields around the closed-ended displacement pile driven in sand. Can Geotech J 61(3):549–561

[9] Harder LF, Boulanger R (1997) Application of K_σ and K_α correction factors. In: Proceeding of the NCEER workshop on evaluation of liquefaction resistance of soils, pp 167–90

[10] Huang X, Hanley KJ, Zhang Z, et al (2019) Structural degradation of sands during cyclic liquefaction: Insight from DEM simulations. Comput Geotech 114:103139

[11] Jiang M, Zhang W, Sun Y, et al (2013) An investigation on loose cemented granular materials via DEM analyses. Granul Matter 15(1):65–84

[12] Jiang M, Zhang A, Li T (2019) Distinct element analysis of the microstructure evolution in granular soils under cyclic loading. Granul Matter 21(2):1–16

[13] Kolapalli R, Rahman M, Karim M, et al (2023) A DEM investigation on the influence of cyclic and static stress ratios and state variables on the pore water pressure generation in granular materials. J Geotech Geoenviron Eng 149(7):04023043

[14] Li X, Li XS (2009) Micro-macro quantification of the internal structure of granular materials. J Eng Mech 135(7):641–656

[15] Li Z, Wang Y, Ma C, et al (2017) Experimental characterization and 3D DEM simulation of bond breakages in artificially cemented sands with different bond strengths when subjected to triaxial shearing. Acta Geotech 12(5):987–1002

[16] Lin H, Suleiman MT, Brown DG, et al (2015) Mechanical behavior of sands treated by microbially induced carbonate precipitation. J Geotech Geoenviron Eng 142(2):04015066

[17] Liu H, Diambra A, Abell JA, et al (2020) Memory-enhanced plasticity modeling of sand behavior under undrained cyclic loading. J Geotech Geoenviron Eng 146(11):04020122

[18] Liu H, Nagula S, Jostad HP, et al (2024) Considerations for using critical state soil mechanics based constitutive models for capturing static liquefaction failure of tailings dams. Comput Geotech 167:106089

[19] Liu HY, Abell JA, Diambra A, et al (2019) Modelling the cyclic ratcheting of sands through memory-enhanced bounding surface plasticity. Géotechnique 69(9):783–800

[20] Oda M (1982) Fabric tensor for discontinuous geological materials. Soils Found 22(4):96–108

[21] van Paassen LA, Ghose R, van der Linden TJ, et al (2010) Quantifying biomediated ground improvement by ureolysis: large-scale biogrout experiment. J Geotech Geoenviron Eng 136(12):1721–1728

[22] Pan K, Yang Z (2018) Effects of initial static shear on cyclic resistance and pore pressure generation of saturated sand. Acta Geotech 13:473–487

[23] Salahshour S, Ong MC, Skaare B, et al (2022) A perspective of decommissioning methods for bottom-fixed offshore wind turbines. In: International Conference on Offshore Mechanics and Arctic Engineering, American Society of Mechanical Engineers, p V008T09A058

[24] Sang G, Lunn RJ, El Mountassir G, et al (2024) Improving non-uniform gravelly sand using microbially induced carbonate precipitation: an outdoor cubic-meter scale trial by engineering contractors. Eng Geol 343:107791

[25] Sarkis M, Abbas M, Naillon A, et al (2022) Dem modeling of biocemented sand: Influence of the cohesive contact surface area distribution and the percentage of cohesive contacts. Comput Geotech 149:104860

[26] Satake M (1982) Fabric tensor in granular materials. In: IUTAM-Conference on Deformation and Failure of Granular Materials, 1982, pp 63–68

[27] Schmidt S, Wiebicke M, Herle I (2022) On the determination and evolution of fabric in representative elementary volumes for a sand specimen in triaxial compression. Granul Matter 24(4):97

[28] Seed HB, Lee KL (1966) Liquefaction of saturated sands during cyclic loading. J Soil Mech Found Div 92(6):105–134

[29] Shen Z, Jiang M, Thornton C (2016) DEM simulation of bonded granular material. part I: contact model and application to cemented sand. Comput Geotech 75:192–209

[30] Vaid Y, Stedman J, Sivathayalan S (2001) Confining stress and static shear effects in cyclic liquefaction. Can Geotech J 38(3):580–591

[31] Šmilauer V, et al (2015) Yade Documentation 2nd ed. The Yade Project, https://doi.org/10.5281/zenodo.34073, http://yade-dem.org/doc/

[32] Wang R, Cao W, Xue L, et al (2021) An anisotropic plasticity model incorporating fabric evolution for monotonic and cyclic behavior of sand. Acta Geotech 16:43–65

[33] Wei J (2021) DEM exploration of confining stress effect in cyclic liquefaction of granular soils. Comput Geotech 136:104214

[34] Wei J, Xu T, He J (2024) Effect of static shear stress and cyclic loading direction on cyclic behaviors of granular soils by DEM analysis. Comput Geotech 167:106112

[35] Wei X, Yang J (2019) Cyclic behavior and liquefaction resistance of silty sands with presence of initial static shear stress. Soil Dyn Earthq Eng 122:274–289

[36] Wichtmann T, Triantafyllidis T (2016) An experimental database for the development, calibration and verification of constitutive models for sand with focus to cyclic loading: part i—tests with monotonic loading and stress cycles. Acta Geotech 11:739–761

[37] Wu Q, Pan K, Yang Z (2021) Undrained cyclic behavior of granular materials considering initial static shear effect: Insights from discrete element modeling. Soil Dyn Earthq Eng 143:106597

[38] Wu Q, Huang L, Zhao F, et al (2023) Liquefaction behavior of inherently anisotropic sand under cyclic simple shear: Insights from three-dimensional DEM simulations. Soil Dyn Earthq Eng 171:107947

[39] Xiao P, Liu H, Xiao Y, et al (2018) Liquefaction resistance of bio-cemented calcareous sand. Soil Dyn Earthq Eng 107:9–19

[40] Xiao P, Liu H, Stuedlein AW, et al (2019) Effect of relative density and biocementation on cyclic response of calcareous sand. Can Geotech J 56(12):1849–1862

[41] Yang J, Sze H (2011) Cyclic behaviour and resistance of saturated sand under non-symmetrical loading conditions. Géotechnique 61(1):59–73

[42] Yang J, Sze H (2011) Cyclic strength of sand under sustained shear stress. J Geotech Geoenviron Eng 137(12):1275–1285

[43] Yang M, Taiebat M (2024) Effect of anisotropic consolidation on cyclic liquefaction resistance of granular materials via 3D-DEM modeling. J Geotech Geoenviron Eng 150(5):04024028

[44] Yang Z, Pan K (2017) Flow deformation and cyclic resistance of saturated loose sand considering initial static shear effect. Soil Dyn Earthq Eng 92:68–78

[45] Yang Z, Li X, Yang J (2007) Undrained anisotropy and rotational shear in granular soil. Géotechnique 57(4):371–384

[46] Yang Z, Xu T, Chen Y (2018) Unified modeling of the influence of consolidation conditions on monotonic soil response considering fabric evolution. J Eng Mech 144(8):04018073

[47] Zhang A, Dieudonné AC (2023) Effects of carbonate distribution pattern on the mechanical behaviour of bio-cemented sands: A DEM study. Comput Geotech 154:105152

[48] Zhang A, Dieudonné AC (2024) Cementor: A toolbox to generate bio-cemented soils with specific microstructures. Biogeotechnics p 100081

[49] Zhang A, Jiang M, Wang D (2023) Effect of fabric anisotropy on the cyclic liquefaction of sands: Insight from DEM simulations. Comput Geotech 155:105188

[50] Zhang A, Magnanimo V, Cheng H, et al (2024) DEM investigation into the small-strain stiffness of bio-cemented soils. Acta Geotech pp 1–15

[51] Zhang F, Wang C, Chang J, et al (2022) DEM analysis of cyclic liquefaction behaviour of cemented sand. Comput Geotech 142:104572

[52] Zhang L, Evans TM (2020) Investigation of initial static shear stress effects on liquefaction resistance using discrete element method simulations. Int J Geomech 20(7):04020087

[53] Zhao CF, Kruyt NP (2020) An evolution law for fabric anisotropy and its application in micromechanical modelling of granular materials. Int J Solids Struct 196:53–66

[54] Zhao CF, Pinzón G, Wiebicke M, et al (2021) Evolution of fabric anisotropy of granular soils: X-ray tomography measurements and theoretical modelling. Comput Geotech 133:104046

[55] Zhao J, Guo N (2013) Unique critical state characteristics in granular media considering fabric anisotropy. Géotechnique 63(8):695–704